Simulations of fiber spinning and film blowing based on a molecular/continuum model for flow-induced crystallization

Anthony J. McHugh* and A.K. Doufas[1]

Department of Chemical Engineering, University of Illinois at Urbana-Champaign, Urbana IL 61801, USA

(Received March 27, 2001)

Abstract

This paper describes the application of our recently developed two-phase model for flow-induced crystallization (FIC) to the simulation of fiber spinning and film blowing. 1-D and 2-D simulations of fiber spinning include the combined effects of (FIC), viscoelasticity, filament cooling, air drag, inertia, surface tension and gravity and the process dynamics are modeled from the spinneret to the take-up roll device (below the freeze point). 1-D model fits and predictions are in very good quantitative agreement with high- and low-speed spinline data for both nylon and PET systems. Necking and the associated extensional softening are also predicted. Consistent with experimental observations, the 2-D model also predicts a skin-core structure at low and intermediate spin speeds, with the stress, chain extension and crystallinity being highest at the surface. Film blowing is simulated using a "quasi-cylindrical" approximation for the momentum equations, and simulations include the combined effects of flow-induced crystallization, viscoelasticity, and bubble cooling. The effects of inflation pressure, melt extrusion temperature and take-up ratio on the bubble shape are predicted to be in agreement with experimental observations, and the location of the frost line is predicted naturally as a consequence of flow-induced crystallization. An important feature of our FIC model is the ability to predict stresses at the freeze point in fiber spinning and the frost line in film blowing, both of which are related to the physical and mechanical properties of the final product.

1. Introduction

Fiber spinning and film formation are polymer processes of great commercial and technological importance. High-speed non-isothermal melt spinning is associated with a concentrated neck-like deformation and the development of high stresses that result in flow-induced crystallization (FIC). Key features to be captured in any model simulation are: neck-like deformation under high-speed conditions and the associated velocity, stress, crystallinity, orientation and temperature profiles. Likewise, in film blowing, one wishes to be able to predict the location of the frost line and the associated stress at the freeze point, as well as bubble radius, thickness, temperature, crystallinity, and orientation profiles, for given sets of processing conditions. Past models for these processes have attempted to incorporate FIC through single- phase constitutive equations (Newtonian and viscoelastic) that couple the crystallization to the model relaxation times or viscosity. In a recent paper (Doufas *et al.*, 1999), we derived a molecular-based

rheological model for flow-induced crystallization that explicitly accounts for both the untransformed melt phase and the semi-crystalline solid phase. The FIC model has been successfully applied to laboratory rheometric flows (Doufas *et al.*, 1999) and melt spinning (Doufas *et al.*, 2000a,b; Doufas and McHugh, 2001a) and excellent agreement with experimental data was found over a wide range of processing conditions and materials. The purpose of this paper is to review the FIC model and illustrate its application to the simulation of fiber spinning and film blowing.

2. Model and equations

Figure 1 shows a sketch of our two-phase model for FIC. The melt (untransformed phase) is modeled as a modified Giesekus fluid with finite chain extensibility, characterized by the conformational tensor c. The semi-crystalline phase is approximated as a collection of rigid rods that grow and orient in the flow field, and is characterized by the orientational tensor S and the equilibrium degree of crystallinity, ϕ_∞. Brackets of a quantity denote averaging with respect to the appropriate diffusion equation distribution function. Crystallization under conditions of both under-cooling and deformation results in the transfer of statistical
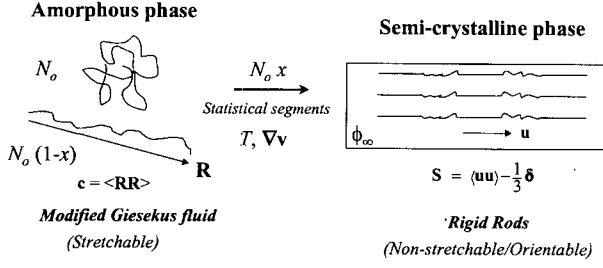
Fig. 1. Schematic representation of molecular-based model for flow-induced crystallization.

segments from the melt to the semi-crystalline phase. The mass fraction of statistical segments in the semi-crystalline medium (degree of transformation), x, is given by N/N_o, where N is the number of statitistical segments in the semi-crystalline phase at any time during the transformation and N_o is the number of statistical segments initially in the melt. The crystallization rate is approximated by a non-isothermal Avrami/Nakamura equation modified with a frame-invariant enhancing factor related to the stored free energy to mimic the effect of flow on the kinetics of the phase transition. Relaxation times of both phases are assumed to be functions of crystallinity and temperature. In what follows, the defining equations of the model and associated transport balances for fiber spinning are most conveniently expressed in terms of the dimensionless variables defined in the Appendix.

2.1. Evolution equations

The evolution equations for the microstructural variables c, S and x are summarized below.

$$c^*_{(1)} = -\frac{1-x}{\lambda_a(x,T)}\left[(1-\alpha)\delta+\frac{\alpha E}{1-x}c^*\right]\cdot\left(\frac{\alpha E}{1-x}c^*-\delta\right) \tag{1}$$

$$S_{(1)} = -\frac{\sigma}{\lambda_{sc}(x,T)}S+\frac{1}{3}[\nabla v+(\nabla v)^T]-2(\nabla v)^T:\langle uuuu\rangle \tag{2}$$

$$\frac{Dx}{Dt} = mK_{av}(T)(1-x)[-\ln(1-x)]^{(m-1)/m}\exp(\xi tr\tau^*) \tag{3}$$

The superscript * denotes a dimensionless quantity, (see Appendix for non-dimensionalizations) the subscript (1) denotes the upper convected derivative, and D/Dt denotes the substantial derivative. δ is the identity tensor, α is the molecular (Giesekus) parameter, σ is an anisotropic drag parameter of the semi-crystalline phase, λ_a, λ_{sc} are the amorphous and semi-crystalline relaxation times, respectively, E is the non-linear spring force factor, u is the unit vector along the semicrystalline rod axis (Fig. 1), K_{av} is the temperature dependent Avrami constant under quiescent conditions, m is the Avrami exponent under flow conditions, and ξ is a model parameter. In the absence of a fundamental theory, m is set equal to

unity to capture the lowering of growth dimensionality under flow. The dependence of the system relaxation times on the transformation are assumed to be as follows:

Melt phase: $\lambda_a(x,T) = \lambda_{a,o}(T)(1-x)^2$ (4)

Semi-crystalline phase: $\lambda_{sc}(x,T) = c\lambda_{a,o}(T)\exp(Fx)$ (5)

where $\lambda_{a,o}$ is the characteristic Hookean relaxation time of the melt (temperature dependent) in the absence of crystallization and c and F are model parameters discussed in Doufas et al (2000a). The melt relaxation time is obtained from the zero-shear viscosity assuming constant shear modulus.

2.2. Extra stress tensor

The expressions for the extra stress tensor are derived based on polymer kinetic theory principles. Prior to the onset of crystallization, the extra stress is given by

$$\tau^* = Ec^* - \delta \tag{6}$$

where E is obtained from the inverse Langevin function (Doufas *et al.*, 1999).

After the onset of crystallization, the total extra stress is calculated from:

$$\tau^* = \frac{E}{1-x}c^*-\delta+3S+6Deb_{sc}(\nabla^*v^*)^T:\langle uuuu\rangle \tag{7}$$

where the Deborah number for the semi-crystalline phase, Deb_{sc}, is given by $Deb_{sc}=v_o\,\lambda_{sc}/L$. In Eq. (7), the dyad product is calculated using a hybrid decoupling approximation:

$$(\nabla^*v^*)^T:\langle uuuu\rangle \cong (1-w)\cdot\left\{\begin{array}{l}\frac{1}{15}(\nabla^*v^*+(\nabla^*v^*)^T)\\[4pt]+\frac{1}{7}[(\nabla^*v^*)^T:S\delta\\[4pt]+S\cdot(\nabla^*v^*+(\nabla^*v^*)^T)+(\nabla^*v^*+(\nabla^*v^*)^T)\cdot S\end{array}\right\}$$

$$+w(\nabla^*v^*)^T:S\left(S+\frac{1}{3}\delta\right) \tag{8}$$

$$w = 1-27\det\left(S+\frac{1}{3}\delta\right) \tag{9}$$

The total extra stress tensor τ^* is expressed in terms of the microstructural variables c^*, S and x through Eqs. (1-3).

The model equations, along with the macroscopic transport equations (mass, momentum and energy) for the polymer process, contain quantities and parameters that fall into 3 categories: (i) properties that can be determined a-priori from measurements of the melt. These include the rheological properties of the melt (zero-shear-rate viscosity, 0_o,

α, and G, the shear modulus), physical properties such as the polymer density, thermal conductivity, surface tension and heat capacities, and quiescent crystallization parameters, such as the equilibrium melting point, T_m°, and the Avrami crystallization parameter (K_{av}), (ii) variables that relate to the processing conditions being modeled, and, (iii) parameters that are material dependent and are calibrated from experimental data for the given process. These include the model parameters, c and F, which are related to the assumed dependence of the semi-crystalline phase relaxation time on the degree of transformation (Eq. 5), the crystallization rate-enhancement factor, >, and the rigid rod anisotropy factor, σ. Model predictions (velocity, temperature, stress profiles and location of freeze point) are most sensitive to the parameters F and >. Extensive discussions of the evaluation of these variables and parameters, and a listing of values used for modeling the melt spinning of the nylons and PET summarized in the next sections, are given elsewhere (Doufas et al., 2000a,b; Doufas and McHugh, 2001a).

3. Simulation of fiber spinning

Figure 2 shows a schematic of the fiber spinning process, illustrating the relevant system variables which are the fiber diameter, temperature, and axial spin line velocity profiles.
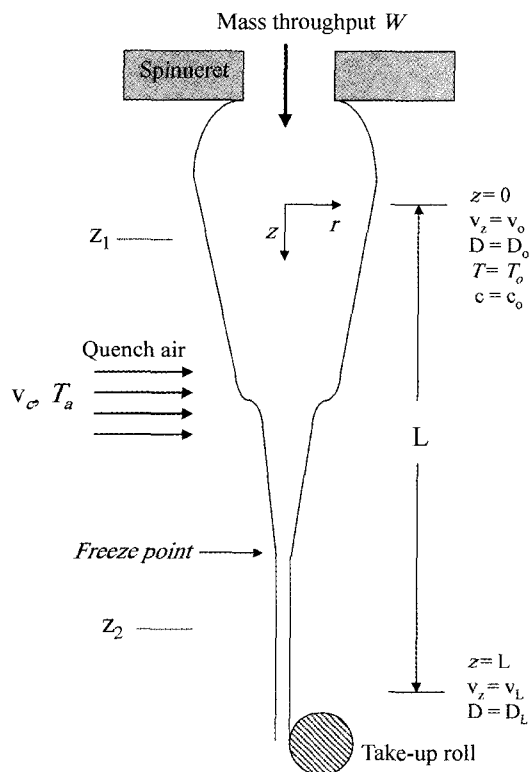

Mass throughput W

Fig. 2. Schematic of fiber spinning process with system variables.

The quench air velocity, v_c, and temperature, T_a, are also important process variables. Shear stresses developed in the spinneret are assumed to have relaxed at the point of maximum die swell ($z = 0$), and the flow field during spinning (0 # z # L) is considered to be a locally homogeneous uniaxial extension. Polymer melt exits the spinneret at a mass flow rate, W. The combination of uniaxial tensile forces acting on the filament during flow and the cooling of the spinline will induce crystallization (at a point where the filament temperature drops below T_m°), and an eventual locking-in of the fiber diameter at the freeze point. The spinline tension varies along the fiber length due to the combined effects of air drag and inertia, and is also strongly influenced by structural changes brought about by the flow-induced crystallization. For high-speed conditions, a concentrated deformation (necking) process occurs over some short region of the spin line, immediately prior to the freeze point, after which filament deformation ceases and the neck stabilizes.

The dimensionless equations for the cross-sectional averaged (thin filament approximation) steady state transport balances are the following

Momentum balance

$$D_1 \frac{dv_z^*}{dz^*} = \frac{d}{dz^*}\left[\frac{\tau_{zz}^* - \tau_{rr}^*}{v_z^*}\right] - D_2(v_z^* - v_r) + \frac{D_3}{v_z^*} - D_4(v_z^*)^{-3/2}\frac{dv_z^*}{dz^*}$$

(10)

where D_1, D_2, D_3, D_4, and v_r are dimensionless quantities defined in the Appendix. The momentum balance includes all relevant effects. The term on the left accounts for inertia, while the terms on the right arise, respectively, from the area-averaged tensile force, air drag, gravity, and surface tension.

Equation of energy

$$\frac{dT^*}{dz^*} = -D_5(v_z^*)^{-1/2}(T^* - T_r) + D_6\frac{\tau_{zz}^* - \tau_{rr}^*}{v_z^*}\frac{dv_z^*}{dz^*} + D_7\frac{dx}{dz^*}$$

(11)

where D_5, D_6, D_7, and T_r are dimensionless quantities defined in the Appendix. The three terms on the right hand side include heat transfer by convection, viscous dissipation, and crystallization, respectively. The overall heat capacity in the parameters, D_5-D_7, is temperature and crystallinity dependent in general (Doufas et al., 2000a,b; 2001a). Substitution of the constitutive equations into the transport equations leads to a set of highly coupled, nonlinear differential equations for the microstructural variables (c^* and S tensors and x) and the macroscopic velocity and temperature fields. These are solved as an initial value problem with a fourth-order, Runge-Kutta algorithm combined with a shooting method (Doufas et al., 2000a,b; Doufas and McHugh, 2001a).

3.1. Fiber spinning results

Figures 3 and 4 show examples of the fit of model predictions to data for high speed spinning of nylon and PET, respectively. In both cases, the model is able to accurately capture the large rise in velocity or equivalent drop in diameter associated with necking. Figure 3 also shows that at a given take-up speed, increasing the mass flow rate moves the freeze point (i.e., the point where the velocity reaches a plateau) away from the spinneret. Flow birefringence, Δn, in Fig. 4 was calculated from the degree of transformation x and the microstructural tensors c, S
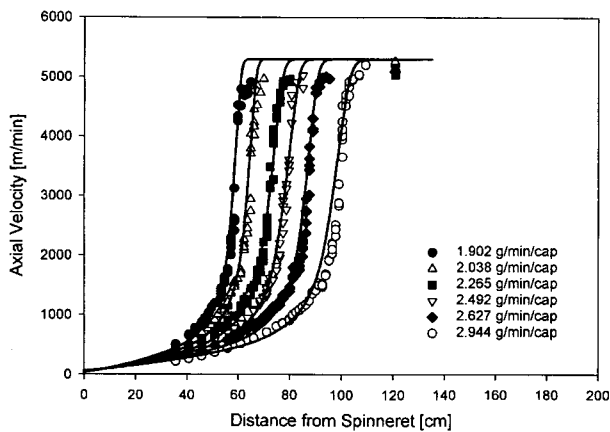
Fig. 3. Profiles of axial velocity under high-speed conditions for nylon melts for various capillary mass flow rates (take-up speed 5300 m/min). Solid lines are model predictions. Data from Doufas et al. (2000 b).
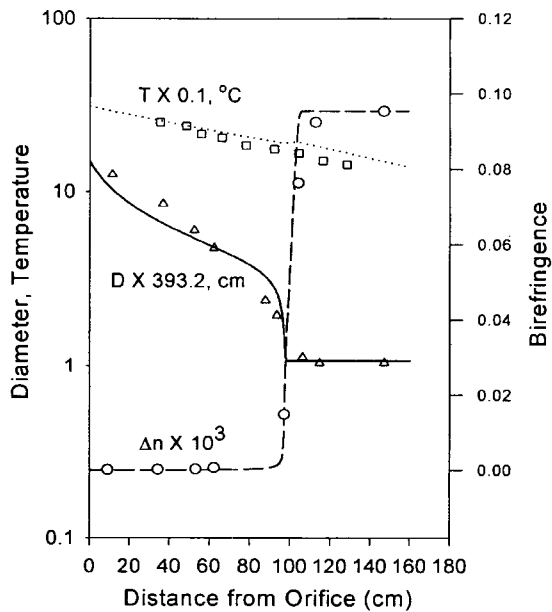
Fig. 4. High-speed diameter, temperature and birefringence profiles for a PET melt. Take-up speed is 5947 m/min and mass flow rate is 4.7 g/min/cap. Data from Vassilatos et al. (1985). The lines represent model predictions.

according to the methodology described previously (Doufas et al., 2000b). The final expression used for the birefringence reads:

$$\Delta n = (1-x)\left(1-\frac{1}{E}\right)\frac{c_{zz}-c_{rr}}{tr\,c}\Delta_m^0+x\frac{3}{2}S_{zz}\,\Delta_{sc}^0 \qquad (12)$$

where Δ_m^0 is the melt intrinsic birefringence and Δ_{sc}^0 is the "apparent" intrinsic birefringence of the semi-crystalline phase. A value of 0.275 for Δ_m^0 (Ziabicki et al., 1998) was used in the calculations and its dependence on temperature was neglected. Δ_{sc}^0 is estimated from the final (plateau) experimental value of the birefringence in the spinline corresponding to $x \approx 1$ (complete transformation). Figures 3 and 4 show the very good fitting and predictive capability of the model under high-speed conditions for both nylon and PET. In consistency with the behavior of nylon (Haberkorn et al., 1993; Doufas et al., 2000a,b), in the neck region, only a small fraction of crystallization actually occurs before the polymer deformation is complete (Fig. 5). This small amount of crystallinity is sufficient to reduce the chain mobility, impose the constraint of non-stretchibility into the system and thereby lead to pinning (stabilization) of the neck. As shown in Fig. 5, most of the crystallization occurs below the neck. Similar crystallinity profiles result for the nylon system (Doufas et al., 2000a,b).

Examples of the model predictions of tensile stress and apparent elongational viscosity profiles for nylon simulations are shown in Fig. 6. Similar results are found for PET (Doufas and McHugh, 2001a). Tensile stress is given as the first normal stress difference, $\tau_{zz} - \tau_{rr}$, and the elongational viscosity is given as the ratio of the tensile stress to the axial velocity gradient, dv_z/dz In consistency with the velocity profiles, the stress profiles for low spin speeds are smooth and the rate of increase levels off after a distance of about 70 cm due to the occurrence of crystallization. The extensional viscosity also shows a monotonic increase
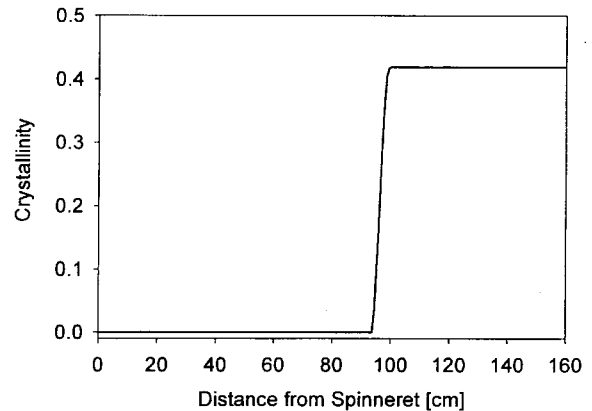
Fig. 5. Predicted crystallinity profile for conditions and model parameters of Fig. 4. Note small amount of crystallinity in the neck region (~95 cm).
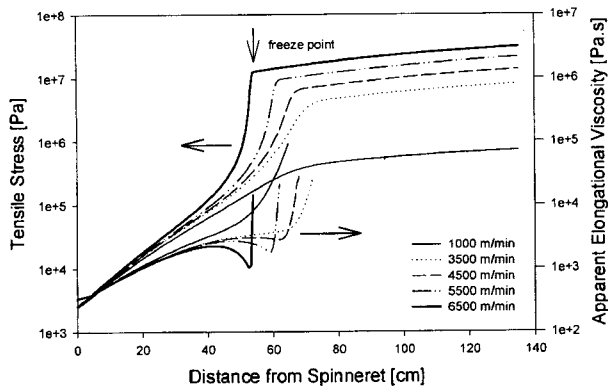
Fig. 6. Effect of take-up speed on tensile stress and apparent elongational viscosity at constant mass throughput for model parameters characteristic of nylon.

Fig. 7. Fit of axial velocity data for low speed spinning of PET for various take-up speeds. Data are from George (1982) and solid lines are model fits.

along the spinline (i.e., no strain softening is predicted which is characteristic of the neck-like deformation at high-speed spinning). At higher take-up speeds (>4500 m/min) the stress shows a sharp rise consistent with the neck-like deformation (see Fig. 3). Near the spinneret, the elongational viscosity is predicted to follow Troutons ratio (ratio of elongational viscosity over shear viscosity is approximately three) for all speeds investigated, implying Newtonian behavior at that location. At small and intermediate distances from the spinneret the apparent elongational viscosity increases with increasing distance from the spinneret and the profiles are nearly independent of take-up speed, reflecting the effect of decreasing temperature on the viscosity and the absence of any significant viscoelasticity. At high spinning speeds (> 4500 m/min), within the neck region, the elongational viscosity profile passes through a maximium, then drops off sharply before rising rapidly again. The presence of the maximum and sharp drop-off reflect the non-linear viscoelasticity, which produces an apparent strain-softening effect. This behavior is consistent with the experimental results of Haberkorn and co-workers (Haberkorn et al., 1993). As shown, the model also predicts the stress at the freeze point (defined as the position along the spinline where the velocity reaches its plateau value), which is believed to be the most important variable related to the physical properties of the as-spun fibers. Comparisons of model predictions with low-speed data of a PET melt are shown in Fig. 7. The predictions are based on the same set of model parameters for all the runs shown. Figure 7 shows the smooth rise of the velocity towards a plateau value, as opposed to the concentrated neck-like deformation shown in Figs. 3 and 4. The freeze point is predicted naturally and corresponds to the development of a very small degree of crystallinity (less than 0.1% (Doufas and McHugh, 2001a) that is still sufficient to lock the system in above the glass transition
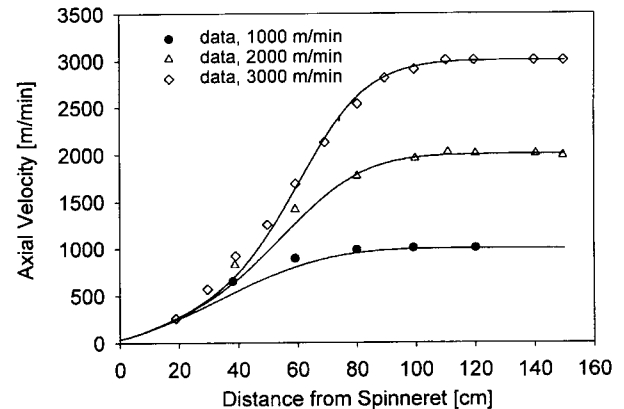
temperature, as opposed to previous approaches which arbitrarily enforce the freeze point at the glass transition temperature.

3.2. Two-dimensional analysis

Application of the microstructural/constitutive model to 2-D simulation of melt spinning, assuming locally uniaxial extensional kinematics in the fiber, has also been carried out (Doufas and McHugh, 2001b). Due to the relatively low thermal conductivity of the polymer (k_p~0.2 W/(m °K)), one expects a radial dependence to develop in the fiber along the spinline. To account for this, one needs to replace the radially averaged energy balance (eqn (11)) with the point-wise 2-D energy equation. Radial resolution of the temperature leads to a radial resolution of the stresses and microstructure (chain extension, molecular orientation and crystallinity) through the dependence of the system relaxation times on temperature, and the dependence of the crystallization rate on both temperature and stress. The combination of these effects inevitably leads to a skin-core structure where the molecular orientation, crystallinity and stress are lowest at the centerline and highest at the surfaces (Shimuzu et al., 1985) which one would like to be able to predict. For low and intermediate spin speeds, one expects radial variations to be smooth enough that the assumption of uniform axial velocity will be accurate. Thus analysis of the fiber spinning problem involves combination of the point-wise 2-D energy equation with the cross-sectionally averaged mass and momentum equations. To carry out the analysis, the free surface domain is mapped to a fixed rectangular computational domain by normalizing the radial coordinate, r, with the fiber radius, R, through the variable $\psi = r/R(z)$. The resulting steady-state dimensionless macroscopic transport equations (combined mass, momentum and energy) of the process are given below.

Momentum balance

$$D_1 \frac{dv_z^*}{dz^*} = \frac{d}{dz^*} \left[\frac{2}{v_z^*} \int_0^1 (\tau_{zz}^* - \tau_{rr}^*) \psi \, d\psi \right] - D_2(v_z^* - v_d^*) + \frac{D_3}{v_z^*}$$

$$-D_4(v_z^*)^{-3/2} \frac{dv_z^*}{dz^*}$$ (13)

The integral on the right hand side of eqn (13) arises from the radial dependence of the stress due to the combination of the temperature dependence of the relaxation times (eqns (4-5)), the radial variation of the temperature (eqn (14)), and the linkage of the stress to the microstructural variables (eqns (1-9)). The remaining terms in eqn (13) are the same as those of eqn (10).

Energy equation

$$\frac{\partial T^*}{\partial z^*} = D_8 \frac{1}{\psi} \frac{\partial}{\partial \psi} \left(\psi \frac{\partial T^*}{\partial \psi} \right) + D_6 \frac{\tau_{zz}^* - \tau_{rr}^*}{v_z^*} \frac{dv_z^*}{dz^*} + D_7 \frac{\partial x}{\partial z^*}$$ (14)

Equation (14) accounts for the radial variation of the temperature through the diffusive term on the right hand side. As with the 1-D simulation, the last term in eqn (14) is zero in the absence of crystallization. In the 2-D simulation, crystallization is assumed to begin at the point along the spinline where the radial-averaged temperature drops below the equilibrium melting point. A complete discussion of the boundary conditions and collocation/Galerkin method used to solve the strongly coupled hydrodynamics/energy and microstructural differential equations is given elsewhere (Doufas and McHugh, 2001b). Material parameters used in the computations were similar to those used in the 1-D simulations and are also discussed in the mentioned references.

3.3. Radial profiles of macroscopic variables (velocity, temperature and tensile stress)

Comparisons of experimental axial velocity and radially averaged temperature profiles for PET and nylon with the model predictions for the real polymer thermal conductivity ($k_p = 0.209$ W/(mK)) and a very large conductivity (10-100 W/(mK) - referred to as infinite conductivity) are shown in Figures 8 and 9, respectively. Predictions of the 2-D model corresponding to infinite thermal conductivity (i.e. $k_p = 10$-100 W/(mK)) were identical to those of the 1-D formulation. The velocity profiles exhibit a smooth increase towards a plateau value and are qualitatively similar, independent of thermal conductivity. As found with the 1-D simulations (Fig 7), the model predicts the occurrence of the freeze point (the point in the spinline below which the axial velocity remains constant) naturally. The velocity profiles exhibit some quantitative difference, which is more pronounced for PET (Figure 8), however the effect of thermal conductivity does not appear to be dra-
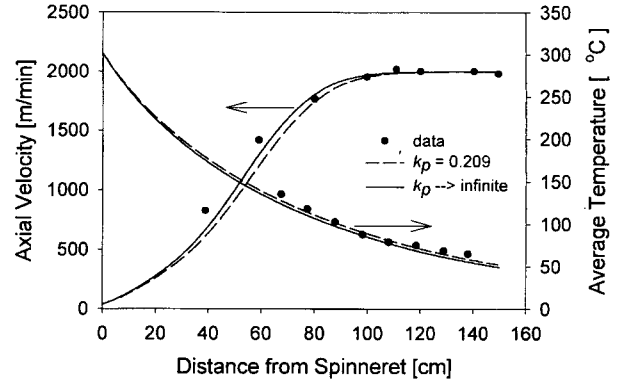

Fig. 8. Comparison of experimental PET velocity and radially averaged temperature profiles with model predictions at low and infinite thermal conductivities. The data were taken from George (1982). The units of thermal conductivity in this and following figures are W/(mK).
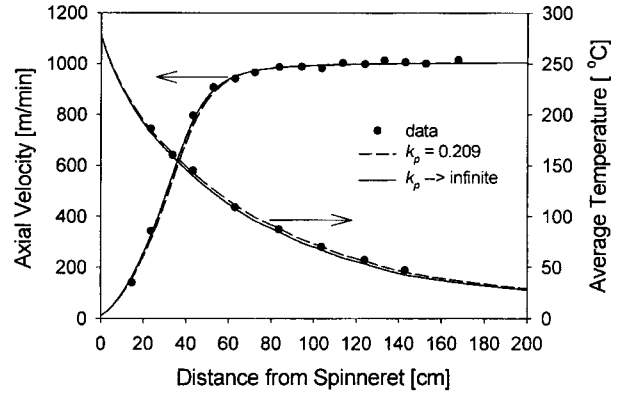

Fig. 9. Comparison of experimental nylon velocity and radially averaged temperature profiles with model predictions at low and infinite thermal conductivities. The data were taken from Doufas *et al.* (2000 b). In this and following figures, the first 200 cm (out of 300 cm) of the spinline are shown.

matic. In general, the experimental profiles are predicted very well, however, as shown in Figures 8 and 9, the predictions corresponding to infinite conductivity are interestingly better than the predictions of the 2-D model corresponding to the low thermal conductivity. This indicates that, although the 1-D formulation does not provide any information about radial gradients, it does do an excellent job in predicting spinline experimental data. Moreover, since the velocity profiles are in excellent agreement with the experimental data, the predicted tensile profiles to be discussed are quite reliable. As will be shown, similar to the 1-D formulation, the 2-D model also predicts the stress below the freeze point down to the take-up roll device naturally, despite the diminishing strain rate. In both cases, the process is simulated from the spinneret to the take-up roll device without the need to impose arbitrary solidification
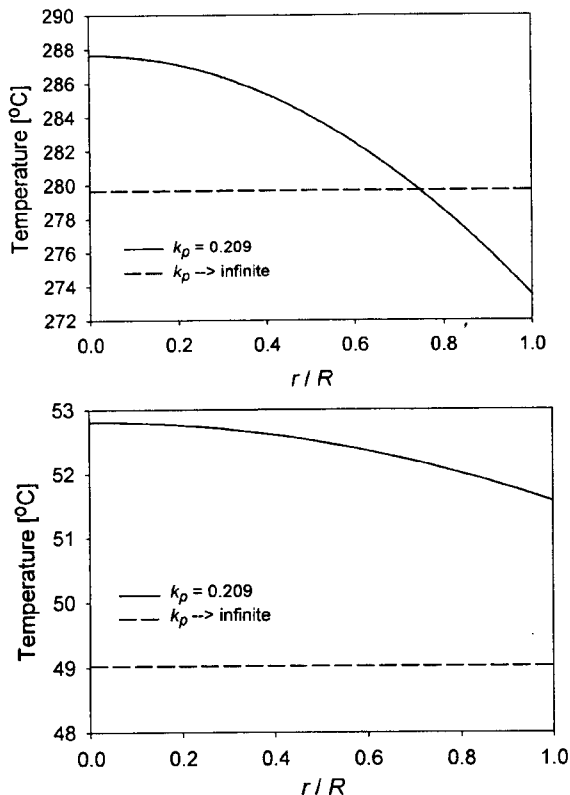
Fig. 10. Temperature radial profiles for PET at two axial positions and thermal conductivities. Top: $z = 4.5$ cm, botom: $z = 150$ cm. The curves are model predictions corresponding to the conditions of Figure 7.

Fig. 11. Tensile stress radial profiles for PET at various axial positions and thermal conductivities. Top: $z = 4.5$ cm, bottom: $z = 120$ cm. The curves are model predictions corresponding to the conditions of Figure 7.
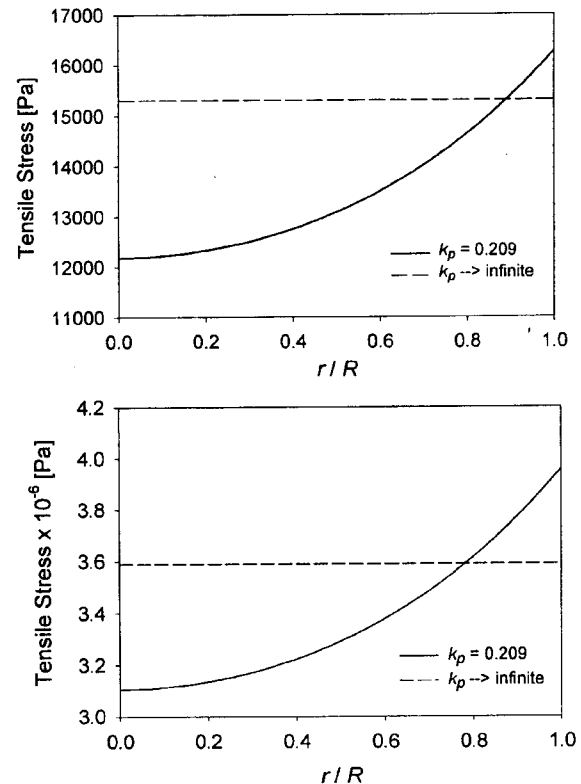
criteria.

The evolution of the predicted radial temperature profiles at two axial positions along the spinline for PET at low thermal conductivity and their comparison with the radially uniform profile at high conductivity, are shown in Figure 10. At the smaller axial distance, the radial resolution is predicted to be higher (14°C difference between the center and surface) and sharper than the radial resolution at the take-up roll at $z = 150$ cm ($1.2°$ difference, i.e. essentially uniform radial profile within experimental error). Therefore, the radial resolution of temperature collapses at relatively large distances from the spinneret, most likely due to the very small fiber diameter. On the other hand, as shown in Figure 11, the tensile force varies radially at the freeze point ($z = 120$ cm) by a factor of 28% relative to the stress at the centerline, despite the collapse of the radial temperature distribution at this location. This is a direct consequence of the radial variation of the microstructural variables, which lock in towards the freeze point, preserving their radial radial non-uniformity, despite the uniformity of the temperature after that point. On the other hand, as also shown in Figure 11, infinite thermal conductivity leads to uniform stress and therefore uniform

properties.

3.4. Radial distribution of microstructure
Amorphous microstructure

Radial resolution of the amorphous chain extension relative to the quiescent coiled state (relative extension, RE) is computed using the following

$$RE = \sqrt{\frac{tr\ c^*}{3(1-x)/E_q}} \tag{15}$$

where E_q is the non-linear force factor under quiescent conditions. The factor $E_q/(1-x)$ corrects for the loss of amorphous statistical strands due to crystallization and the deviation of the amorphous chains from the Gaussian distribution under flow conditions. Profiles of the relative extension along the spinline at the fiber center and the surface at low thermal conductivity, as well as the uniform profile at infinite thermal conductivity, for PET are illustrated in Figure 12. The profiles are qualitatively similar, namely the amorphous chains have a random coil configuration at the spinneret exit (RE = 1) consistent with the Newtonian behavior of PET at that location, and the chain extension increases smoothly and locks in after a certain
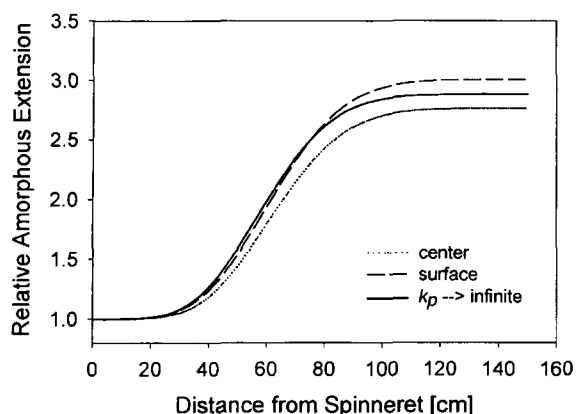
Fig. 12. Profiles of centerline and surface relative amorphous chain extension (k_p = 0.209 W/(mK)), and uniform RE profile ($k_p \to \infty$) along the spinline for PET. The curves are model predictions corresponding to the conditions of Figure 7.
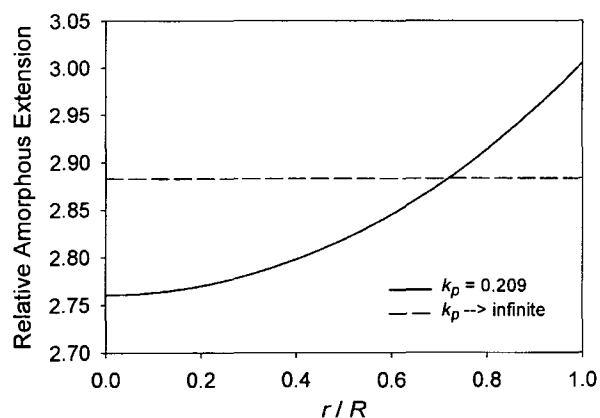

Fig. 13. Relative amorphous extension radial profiles for PET at the take-up roll device (z = 150 cm) at low and infinite thermal conductivities. The curves are model predictions corresponding to the conditions of Figure 7.

distance (vicinity of freeze point) at all radial locations and in the case of $k_p \to \infty$ as well. The chain extension at the surface is predicted to be higher than at the centerline (by a factor of about 9% at the take-up roll), consistent with the tensile stress profiles (Figure 11). Clearly, the model predicts a skin-core structure, which is consistent with experimental observations (Shimizu *et al.*, 1985). This is more clearly illustrated in Figure 13. As noted above, the microstructure preserves its radial variation throughout the spinline, although the temperature radial distribution collapses after a certain distance. This is attributed to the fact that as the system cools and approaches the freeze point, the microstructures of both the amorphous material and the entrapped infinitesimal crystals that formed above the glass transition temperature lock-in. Below the freeze point, although the temperature distribution becomes radially uni-

form, it does not have any effect on the locked-in microstructure. As shown in Figure 13, infinite thermal conductivity results in radially uniform chain extension, reflecting the uniform temperature profile (Figure 11). Therefore, finite thermal conductivity leads to radially non-uniform amorphous microstructure, which is irreversible, i.e., it does not convert to uniform despite the eventual temperature uniformity over the fiber cross-section at low thermal conductivity. Profiles of the orientation factor of the infinitesimal crystals are similar to the profiles of the relative extension (Doufas and McHugh, 2001b).

An interesting observation, independent of thermal conductivity, is that the overall (macroscopic) amount of stretch experienced by the filament, calculated from the ratio of the take-up velocity to the velocity at the spinneret exit (draw ratio ≈ 53), is considerably higher than the molecular stretching (RE ≈ 3 at the end of the spinline). This behavior is attributed to extensive slippage of the entanglements within the polymer network (viscoelastic behavior).

Semi-crystalline microstructure

The semi-crystalline orientation factor f_{sc}, which gives the average molecular orientation of the semi-crystalline phase with respect to the z- axis, is calculated in our model as follows:

$$f_{sc} = \sqrt{\frac{3}{2} \boldsymbol{S} : \boldsymbol{S}} = \frac{3}{2} S_{zz} \tag{16}$$

The evolution of the centerline, surface and average f_{sc} profiles together with the uniform f_{sc} profile at $k_p \to \infty$, along the spinline for nylon are demonstrated in Figure 14. All the profiles are similar qualitatively; at small distances below the spinneret the molecular orientation of the infinitesimal crystals is isotropic ($f_{sc} \approx 0$) and develops smoothly along the spinline following the flow deformation, and finally locks-in at the vicinity of the freeze point reaching a plateau value. The uniform orientation profile corresponding to $k_p \to \infty$ is predicted to approach the cross-sectionally averaged profile corresponding to low k_p and the plateau average orientation practically coincides with the plateau uniform orientation, reflecting the behavior of the tensile stress. Due to the locking-in of the microstructure caused by the filament cooling and crystallization that prevent the molecules from relaxing, the molecular orientation preserves its radial non-homogeneity (Figures 14, 15) despite the collapse of the temperature radial profile at large distances from the spinneret. The same is true for the crystallinity profiles shown in Figures 16, 17. While the model predicts a radially uniform molecular orientation in the limit $k_p \to \infty$ (Figure 17) due to radial homogeneity of the temperature, in the case of low thermal conductivity the orientation at the surface is higher relative to the centerline orientation (by a factor of about 50% at z = 150 cm) sup-
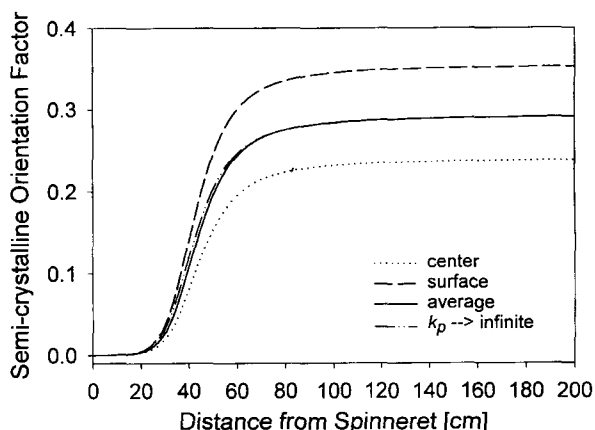
Fig. 14. Profiles of centerline, surface and average semi-crystalline orientation factor f_{sc} [$k_p = 0.209$ W/ (mK)], and uniform f_{sc} profile ($k_p \rightarrow \infty$) along the spinline for nylon. The curves are model predictions corresponding to the conditions of Figure 8.

Fig. 16. Profiles of centerline, surface and average degree of transformation x [$k_p = 0.209$ W/(mK)], and uniform x profile ($k_p \rightarrow \infty$) along the spinline for nylon. The curves are model predictions corresponding to the conditions of Figure 8.
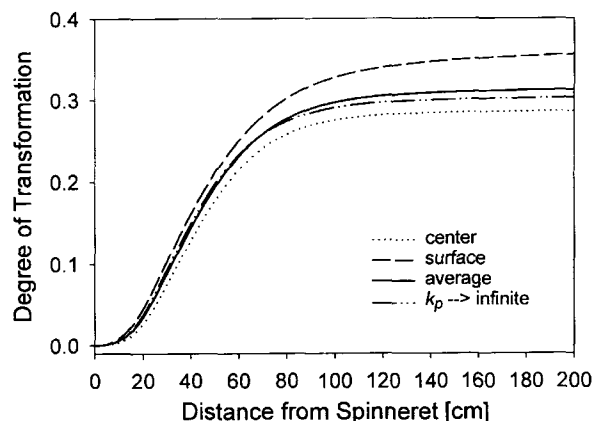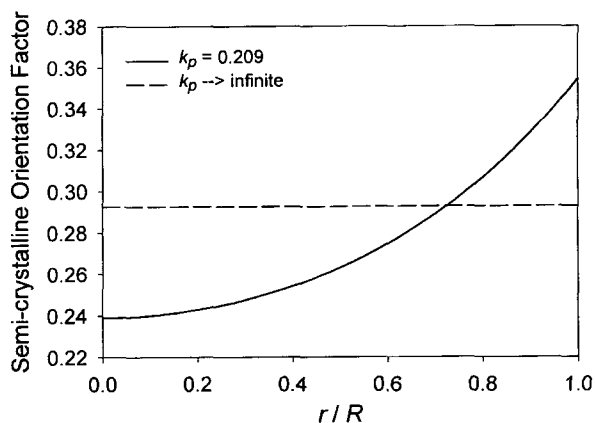

Fig. 15. Semi-crystalline orientation factor radial profile for nylon at the take-up roll device ($z = 300$ cm) at low and infinite thermal conductivities. The curves are model predictions corresponding to the conditions of Figure 8.

Fig. 17. Degree of transformation radial profile for nylon at the take-up roll device ($z = 300$ cm) at low and infinite thermal conductivities. The curves are model predictions corresponding to the conditions of Figure 8.
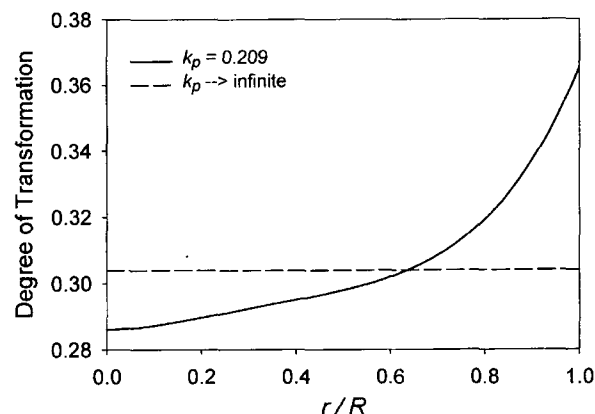
porting the formation of a skin-core structure. The skin-core structure is further evidenced by prediction of higher crystallinity at the surface than the centerline. At the take-up roll device, the crystallinity at the surface is higher by a factor of about 22% relative to the centerline. This behavior of the crystallinity is consistent with the lower temperature and higher tensile stress and molecular orientation at the surface, both factors contributing to higher crystallization rates. The radial variation for both orientation and crystallinity is minimum (radial gradients approach zero) towards the centerline, consistent with zero temperature radial gradients at this location, and becomes highest at the surface (the radial gradients are steepest at the surface as expected). These results further enhance the statement that if one is interested in predicting the average fiber properties

in the cross-sectional area, the 1-D formulation should be sufficient. However, if the radial resolution of the fiber properties is important, our 2-D formulation can provide such information through the radial variation of the microstructural variables. Thus, the model can provide a useful link between microstructure development and final fiber properties.

4. Simulation of film blowing

A schematic of the film blowing process is shown in Fig. 18. Polymer melt exits an annular die at a mass flow rate, W, and is simultaneously stretched in the machine (axial) direction, z, and blown to an inflation pressure ΔP (denoted DP in Fig. 18), while simultaneously being cooled by quench air. The combination of undercooling and flow

Flattened Tube

DP

DR specified

R_L

Freezeline

1

R(z)

2

H(z)

L

z

Cooling Air

r

R = R_o, H = H_o
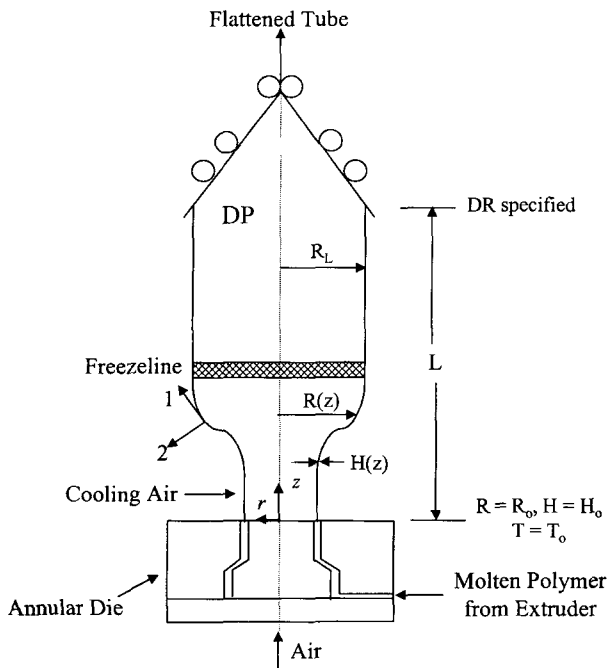T = T_o

Annular Die

Molten Polymer
from Extruder

Air

Fig. 18. Schematic of film blowing process and system variables.

deformation give rise to flow-induced crystallization (FIC) (at a point where the film temperature drops below $T_m^{\,o}$), which stiffens the microstructure, resulting in retardation of the bubble growth and the formation of an essentially constant diameter tube after the frost line.

In order to demonstrate the ability of our FIC model to predict the major features of film blowing, a number of simplifying assumptions have been made in our analysis (Doufas and McHugh, 2001c). Inclusion of axial curvature in the momentum balance in the framework of the Petrie and Pearson formalism (Pearson and Petrie, 1970) leads to numerical difficulties in that, beyond a certain degree of crystallinity, the numerical system of equations becomes unstable and/or multiple steady-state solutions can result. Moreover, crystallization is not able to stop the deformation and lead to formation of a constant diameter tube. These difficulties can be overcome by neglecting axial curvature and treating the bubble as a pseudo-cylinder at each position, in line with the work of Liu et al. (1995a,b). Consistent with thin film theory [Novozhilov (1959), Kraus (1967)], we also assume that the total stress in the thickness direction, T_{22}, is zero throughout the film. Thus the polymer isotropic pressure p is the extra stress τ_{22}. The effects of air drag, gravity, inertia, and surface tension are also neglected.

The defining balance equations thus become the following:

Cross-sectionally averaged continuity equation

$$W = 2\pi\rho RHv_1 \tag{17}$$

where ρ is the polymer density, assumed constant in the present study, R is the local bubble radius, H is the local bubble thickness and v_1 is the local velocity in the "1" direction. In the following discussion, we will refer to v_1 as "velocity".

Cross-sectionally averaged momentum equations:

$$F_t = 2\pi RHT_{11} = 2\pi RH(\tau_{11} - \tau_{22}) \tag{18}$$

where F_t is the tensile force in the z direction (constant in all locations) and T_{11} is total axial stress (extra stress and isotropic pressure).

$$\frac{HT_{33}}{R} = \frac{H(\tau_{33}-\tau_{22})}{R} = \Delta P \tag{19}$$

where T_{33} is total hoop stress (extra stress and isotropic pressure).

Cross-sectionally averaged energy equation:

$$\rho C_p \frac{dT}{dz} = -\frac{2\pi R\rho}{W}[U(T-T_a) + \sigma_B \varepsilon(T^4 - T_a^4)] + \boldsymbol{\tau}:\nabla v + \rho\Delta H_f \frac{d\phi}{dz} \tag{20}$$

In Eq. (20), C_p is the heat capacity, U is the convective heat transfer coefficient, σ_B is the Stefan-Boltzmann constant and ε is the emissivity. The second term on the RHS expresses the viscous dissipation, and the last term is related to the release of latent heat, with ΔH_f being the heat of crystallization per unit mass, and ϕ (= $x\phi_\infty$, where ϕ_∞ is the final degree of crystallinity, and x, as before, is the degree of transformation) is the average *absolute* degree of crystallinity of the system (mass fraction of crystals) at the axial position z. In the absence of crystallization, the last term on the RHS of Eq. (20) vanishes. Axial conduction and radiation effects are also neglected.

Neglecting axial curvature, the velocity gradient tensor ∇v, becomes the following:

$$\nabla v = \frac{w}{2\pi\rho RH}\begin{bmatrix} \left(-\frac{1}{H}\frac{dH}{dz}\right)-\frac{1}{R}\frac{dR}{dz} & 0 & 0 \\ 0 & \frac{1}{H}\frac{dH}{dz} & 0 \\ 0 & 0 & \frac{1}{R}\frac{dR}{dz} \end{bmatrix} \tag{21}$$

Similar to the fiber spinning analysis, the highly non-linear, coupled equations for the system variables that result from substitution of Eqs. (17) - (21) into Eqs. (1) - (3) are solved using a Runge-Kutta integration scheme together with a shooting method. Details are given in Doufas and McHugh (2001c). Simulation results to be shown were carried out for a LDPE melt with zero-shear viscosity of 1.53×10^4 Pa.s and relaxation time of 0.85 s at 190°C. In all cases, the mass flow rate was 0.15 g/s, the draw ratio was

10

set to 4, the bubble radius and thickness were 0.746 cm and 0.95 mm at the exit of the die, respectively, and the axial length from the die up to the nip rolls was L = 82 cm. When the effect of a processing condition is investigated, all other conditions and model parameters are kept constant.

4.1. Film blowing results

Figure 19 shows the effect of inflation pressure on the bubble shape. For an inflation pressure of 250 Pa, the bubble is predicted to expand, for 185 Pa the radius remains more or less constant, and for the lower pressures of 50 Pa and 0 Pa, the bubble is predicted to contract. These results are consistent with the experimental data of Liu et al. (1995a,b). In the limit of zero inflation pressure, our model predicts that the bubble experiences uniaxial extension kinematics (it contracts equally in the hoop and thickness directions), which is also in agreement with the experimental data of Han and Park (1975).

The dynamics of the temperature and degree of transformation profiles for the numerical experiment with $\Delta P =$
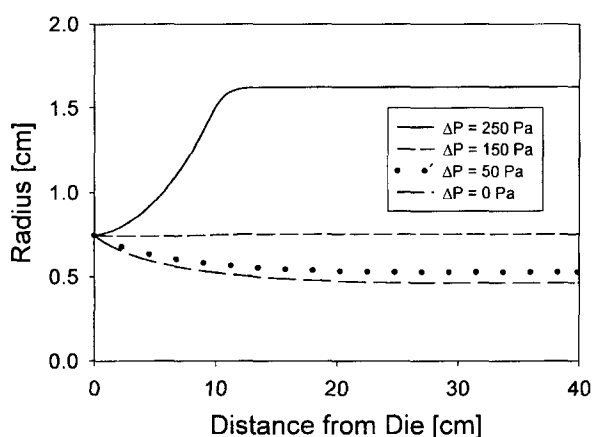

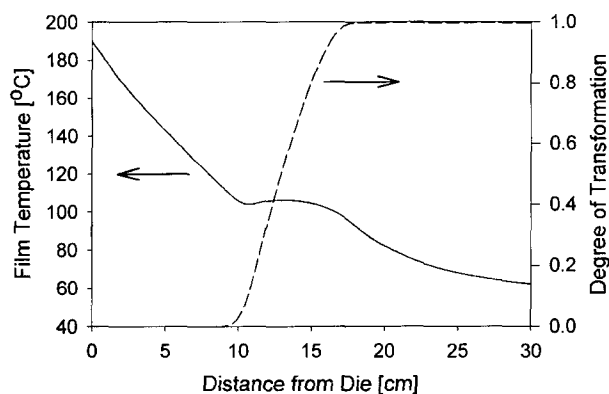Fig. 19. Effect of inflation pressure on bubble shape. $T_o = 190°C$, DR = 4.

Fig. 20. Dynamics of film temperature and crystallinity, for $T_o = 190°C$, DR = 4, and $\Delta P = 345$ Pa.

345 Pa were also evaluated. As shown in Fig. 20, the film temperature initially decreases due to quench air cooling, however beyond a distance above the die (~10 cm), the temperature plateaus and increases slightly due to the release of latent heat of crystallization which dominates the cooling effect. Upon completion of crystallization (100% degree of transformation and 44% absolute crystallinity), the temperature drops again due to cooling. Similar to fiber spinning, a small amount of crystallinity (~0.01) is able to stop the deformation and lead, in this case, to the formation of a constant bubble diameter for all the inflation pressures indicated. In the case of $\Delta P = 345$ Pa, crystallization takes place mostly after the frost line at about 10 cm, i.e., after the point at which the diameter remains constant, similar again to the behavior shown with fiber spinning. It is important to note the freeze line is predicted naturally in our formulation as a result of the coupling of crystallization with the rheological behavior of the semi-crystalline system and the macroscopic equations of the process. Moreover, in our formalism, we simulate the process from the die up to the nip rolls and the length of the domain does not cause any instabilities.

The extra stress differences, τ_{11}-τ_{22} and τ_{33}-τ_{22} for $\Delta P = 345$ Pa are found to increase due to the deformation experienced by the bubble and they remain constant after the freezeline, at about 10 cm. This is a direct consequence of crystallization which stops the deformation and locks the stresses and microstructure. The stresses at the frost line are inextricably related to the physical and mechanical properties of the final film.

With regard to the effect of extrusion temperature on the dynamics of the bubble radius and thickness, at the higher extrusion temperatures, the bubble is found to be more deformable and therefore to expand more [Doufas and McHugh (2001c)]. In fact, both the BUR and thickness reduction are found to increase with increasing temperature. At lower temperatures, the polymer is too stiff to expand radially and the BUR is found to be close to unity. These predictions are also qualitatively consistent with the experimental observations of Liu et al. (1995a,b).

Acknowledgements

References

Doufas, A. K, I.S. Dairanieh, and A.J. McHugh, 1999, A con-

tinuum model for flow-induced crystallization of polymer melts, *J. Rheol.* **43**, 85-109.

Doufas, A. K, A.J. McHugh, and C. Miller, 2000a, Simulation of melt spinning including flow-induced crystallization. Part I. Model development and predictions, *J. Non-Newt. Fluid Mech.* **92**, 27-66.

Doufas, A. K, A.J. McHugh, C. Miller, and A. Immaneni, 2000b, Simulation of melt spinning including flow-induced crystallization. Part II. Quantitative comparisons with industrial spinline data, *J. Non-Newt. Fluid Mech.* **92**, 81-103.

Doufas, A.K. and A.J. McHugh, 2001a, Simulation of melt spinning including flow-induced crystallization. Part III. Quantitative comparisons with PET spinline data, *J. Rheol.* **45**, 403-420.

Doufas, A.K. and A.J. McHugh, 2001b, Two-dimensional simulation of melt spinning with a microstructural model for flow-induced crystallization, *J. Rheol.*

Doufas, A.K. and A.J. McHugh, 2001c, Simulation of film blowing including flow-induced crystallization. Part III. Quantitative comparisons with PET spinline data, *J. Rheol.* **45**, 403-420.

George, H.H. 1982, Model of steady-state melt spinning at intermediate take-up speeds, *Polym. Eng. Sci.* **22**, 292-299.

Haberkorn, H., K. Hahn, H. Breuer, H.-D. Dorrer, and P. Matthies, 1993, On the neck-like deformation in high-speed spun polyamides, *J. Appl. Polym. Sci.* **47**, 1551-1579.

Han, C. D. and Park, J. Y., 1975, Studies on blown film extrusion. II. Analysis of the deformation and heat transfer processes, *J. Appl. Polym. Sci.* **19**, 3277.

Kraus, H., 1967, *Thin elastic shells*, Wiley, New York.

Liu, C.-C., D.C. Bogue, and J.E. Spruiell, 1995a, Tubular film blowing. Part 1. On-line experimental studies, *Intern. Polym. Proc.* **10**, 226-229.

Liu, C.-C., D.C. Bogue, and J.E. Spruiell, 1995b, Tubular film blowing. Part 2. Theoretical modeling, *Intern. Polym. Proc.* **10**, 230-236.

Novozhilov, V.V., 1959, *The Theory of Thin Shells*, Noordhoff, Groningen.

Pearson, J.R.A. and C.J.S. Petrie, 1970, The flow of a tubular film. Part 2. Interpretation of the model and discussion of solutions, *J. Fluid Mech.* **42**, 609-625.

Shimizu, J., N. Okui, and T. Kikutani, 1985, in *High-speed fiber spinning, science and engineering aspects*, edited by A. Ziabicki and H. Kawai, Wiley-Interscience, New York.

Vassilatos, G., B.H. Knox, and H.R.E. Frankfort, 1985, in *High-speed fiber spinning, science and engineering aspects*, edited by A. Ziabicki and H. Kawai, Wiley-Interscience, New York.

Ziabicki A., L. Jarecki, A. Wasiak, 1998, Dynamic modelling of melt spinning, *Comput. Theor. Polym. Sci.* **8**, 143-157.

Appendix

A number of dimensionless variables and quantities used in the model equations are described below.

Dimensionless axial distance and ∇ *operator :*
$z^* = z/L,\ \nabla^* = \nabla/L$

Dimensionless velocity : $v_z^* = v_z/v_o$

Dimensionless temperature : $T^* = T/T_o$

Dimensionless c tensor : $c^* = cK_o/k_BT$, where K_o is the Hookean spring constant of the melt chains before the onset of crystallization [Doufas *et al.* (2000a)] and k_B is the Boltzman constant.

Dimensionless extra stress tensor : $\tau^* = \tau/G$, where G is the melt shear modulus, given by $G = nk_BT$, where n is the number density of molecules in the system.

Inertia : $D_1 = \dfrac{\rho v_o^2}{G}$

Air drag : $D_2 = \dfrac{\Pi\mu_a BL\rho\ v_o^2}{GW}$, where W is the mass flow rate, B is the Bingham number and μ_a is the quench air viscosity [Doufas et al. (2000a)].

Gravity : $D_3 = \dfrac{gL\rho}{G}$, where g is the acceleration of gravity.

Surface tension : $D_4 = \left(\dfrac{\pi s^2 \rho v_o}{4WG^2}\right)^{1/2}$, where s is the surface tension.

Heat convection : $D_5 = \left(\dfrac{4\pi L^2 h^2}{\rho C_p^2 v_o W}\right)^{1/2}$, where h is the convective heat transfer coefficient and C_p is the system heat capacity which will depend on temperature and the degree of transformation [Doufas et al. (2000b), Doufas and McHugh (2001a)].

Viscous dissipation : $D_6 = \dfrac{G}{\rho C_p T_o}$

Latent heat of crystallization : $D_7 = \dfrac{\Delta H_f\ \phi_\infty}{C_p T_o}$, where ΔH_f is the heat of crystallization per unit mass.

Polymer thermal conductivity : $D_8 = \dfrac{\pi L k_p}{C_p W}$,

Relative velocity : $v_r = \dfrac{v_d}{v_o}$, where v_d is the axial component of the quench air velocity (taken to be zero in the present study).

Relative temperature : $T_r = \dfrac{T_a}{T_o}$